PHYSICAL REVIEW FLUIDS **4**, 044606 (2019)

Are extreme dissipation events predictable in turbulent fluid flows?

Patrick J. Blonigan
NASA Ames Research Center, Moffett Field, California 94035, USA

Mohammad Farazmand[*] and Themistoklis P. Sapsis[†]
Department of Mechanical Engineering, Massachusetts Institute of Technology, Cambridge, Massachusetts 02139, USA

(Received 26 July 2018; published 17 April 2019)

We derive precursors of extreme dissipation events in a turbulent channel flow. Using a recently developed method that combines dynamics and statistics for the underlying attractor, we extract a characteristic state that precedes laminarization events that subsequently lead to extreme dissipation episodes. Our approach utilizes coarse statistical information for the turbulent attractor, in the form of second-order statistics, to identify high-likelihood regions in the state space. We then search within this high-probability manifold for the state that leads to the most finite-time growth of the flow kinetic energy. This state has both high probability of occurrence and leads to extreme values of dissipation. We use the alignment between a given turbulent state and this critical state as a precursor for extreme events and demonstrate its favorable properties for prediction of extreme dissipation events. Finally, we analyze the physical relevance of the derived precursor and show its robust character for different Reynolds numbers. Overall, we find that our choice of precursor works well at the Reynolds number it is computed at and at higher Reynolds number flows with similar extreme events.

DOI: 10.1103/PhysRevFluids.4.044606

I. INTRODUCTION

Turbulent fluid flows have been the most challenging paradigm of chaotic behavior with signatures of persistent and intermittent (i.e., over finite-times and at arbitrary time instants) instabilities leading to nonlinear energy transfers between scales. These nonlinear energy transfers are responsible for both the broad band character of the spectrum but also for the non-Gaussian statistics. More specifically, while nonzero third order statistics are primarily responsible for the persistent nonlinear energy transfers (turbulent cascades) and the shape of the spectrum [1,2], intermittent events, such as dissipation bursts, are primarily responsible for the heavy tail characteristics [3–7].

Here we are interested in the formulation of precursors for predicting these extreme events. These are important in problems related to atmospheric and climate science, fluid-structure interactions, and turbulent fluid flow control, just to mention a few. We present our analysis on a standard configuration of a turbulent fluid flow, namely the channel flow, that exhibits extreme events in the form of large dissipation episodes occurring in random times [8,9]. These extreme events rise out of a high-dimensional turbulent attractor essentially without any clear warning. They have the form of

---

[*] mfaraz@mit.edu

[†] Corresponding author: sapsis@mit.edu

a short-time excursion towards laminarization of the flow and a subsequent burst of turbulent kinetic energy which leads to a large dissipation episode pushing the flow away from the laminar state.

Many aspects of these intermittent bursts remain elusive primarily because of the intrinsic high dimensionality of the underlying turbulent attractor that limits the applicability of existing mathematical approaches [10,11]. In particular, extreme events due to their rare character cannot be "seen" effectively by energy-based methods, such as proper orthogonal decomposition (POD). Even if one tries to consider conditional POD modes during extreme events these will not necessarily give the modes related to the triggering of the extreme events, as these do not necessarily obtain high energy, even during the extreme event.

A different class of methods focus on the spectral analysis of the underlying Koopman operator [12,13], and strive to extract unstable modes associated with certain observables of the system. Such unstable modes are typically estimated by dynamic mode decomposition (DMD) [14–16]. This analysis, however, can only detect modes associated with long-term instabilities which do not seem to explain short-term intermittent events observed in turbulent flows [17,18]. Other variants, however, such as multi-resolution DMD [19] have been demonstrated to work well in systems with relatively low-dimensional attractors.

Extreme events in complex dynamical systems have also been analyzed recently using large deviation theory (LDT), e.g., in nonlinear water waves [20]. The basic idea is to search the phase space for initial conditions associated with a given magnitude of the objective function (observable of interest) and then from those pick the one with the highest probability of occurrence. However, these efforts have shown to work well in systems where the core of the attractor has Gaussian statistics. For different cases there is no rigorous foundation for LDT to operate. Even in the Gaussian case, the resulting optimization problem has very high dimensionality to be practically solvable for an application like the one considered here—see Ref. [21] for a detailed discussion.

Here we apply a recently developed framework for the discovery of precursors to extreme events [3]. This framework formulates the precursors as solutions to a constrained optimization problem (note that a formally similar approach was presented in Ref. [22] to identify small perturbations of the laminar flow for transition to turbulence). In contrast to LDT, in the present approach we consider a set of high-probability initial conditions, based on a rough approximation of the attractor, and then search within this set for the initial state that has the highest growth for the quantity of interest. An adjoint solver is employed to compute the gradient of the objective function. Because the search is constrained within a low-dimensional (but high-probability) set, the feasibility set, the resulted optimization problem is computationally tractable. The solution provides with an initial state that has high probability to occur and leads to rapid growth of the objective function (in our case the kinetic energy). We discuss the physical relevance of the derived critical state in the context of the turbulent channel flow and use the alignment with this critical state as a scalar precursor for the prediction of future extreme events. We measure the effectiveness of the precursor through direct numerical experiments and examine its robustness over different Reynolds numbers. The success of our approach to an intermittently turbulent channel paves the way for studying transitional flows, such as bypass transition of boundary layers.

This paper is organized as follows. In Sec. II we described the minimal channel flow used in this work and discuss various aspects of the problem. The optimization problem for discovering the precursor to extreme events is presented in Sec. III. In Sec. IV we present a statistical analysis quantifying the predictive power of the optimal precursor. Finally, our concluding remarks are presented in Sec. V.

II. TURBULENT CHANNEL FLOW-PHENOMENOLOGY

A. The minimal flow unit for channel flows

Turbulent channel flow has been a staple of numerical studies of turbulence for many years [8]. The chaotic nature of these simulations makes it difficult to analyze local spatiotemporal events and physical mechanisms in them, such as the formation and destruction of individual hairpin vortices in the near-wall region. To isolate these physical mechanisms and others, work has been done to find "minimal flow units" for various regions of the channel. Jimenez and Moin [23] found the minimal flow unit for near wall turbulence for several low Reynolds number flows by considering turbulent channel flow simulations with domains that were considerably smaller than conventional channel flow simulations. These smaller domains eliminate larger scale turbulent structures but accurately resolved the near-wall turbulent flow, matching turbulent flow statistics from experiments and prior numerical studies up to 40 wall units in the wall-normal direction.

Various minimal flow units have been used in a range of different studies because of its isolation of a few physical mechanisms and its relatively low computational cost. Carlson and Lumley used the minimal flow unit to study flow control strategies for turbulent boundary layers [24]. Minimal flow units have also been used to study near-wall and log-layer turbulence [25–27]. These studies use forcing functions to achieve turbulent flows in half-channels, and to selectively damp larger scale flow structures. Recently, near-wall minimal flow units have been used to study and characterize the effects of wall-roughness on wall-bounded flows and to build models of wall roughness effects [28,29]. The near-wall minimal flow unit has also been used to demonstrate shadowing-based adjoint sensitivity analysis [30].

In addition, the near-wall minimal flow unit simulations routinely show highly intermittent behavior which is of interest for the purposes of our study. In certain low Reynolds number simulations, the flow on one wall exhibits turbulent behavior while the other remains laminar. The flow on both walls transitions at seemingly random intervals: the laminar wall would become turbulent, and then the turbulent wall would become laminar. Turbulent flow in the near-wall minimal flow unit is itself intermittent when it occurs. Time series of wall shear stress show that turbulence undergoes a cycle where it proliferates rapidly or "bursts," then decays slowly. This observation led to numerous subsequent studies into the intermittent nature of near-wall turbulence using minimal flow units (see Refs. [31,32], for comprehensive reviews).

B. Flow solver

In this study we consider near-wall minimal flow units similar to those considered in Ref. [23]. We use a Discontinuous-Galerkin spectral-element method (DGSEM) framework to simulate the minimal flow unit with the compressible Navier-Stokes equations [33]. The DGSEM framework has been successfully applied to a range of different flows including channels flows and the near-wall minimal flow unit [34–36]. Also, it has an adjoint capability [37] that has been validated for the near-wall minimal flow unit in Ref. [30]. A detailed description of the discretization and implementation of this solver is available in Refs. [38] and [39].

We run a direct numerical simulation (DNS) of the channel flow with the compressible Navier-Stokes equations with a constant forcing in the axial direction to drive the channel. Since the Mach number is low, the effective governing equations reduce to the incompressible Navier–Stokes equations,

$$\nabla \cdot \boldsymbol{u} = 0, \tag{1a}$$

$$\partial_t \boldsymbol{u} + \boldsymbol{u} \cdot \nabla \boldsymbol{u} = \frac{f_0}{\rho} \boldsymbol{e}_1 - \frac{1}{\rho} \nabla p + \nu \Delta \boldsymbol{u}, \tag{1b}$$

$$\boldsymbol{u}(\boldsymbol{x}, 0) = \boldsymbol{u}_0(\boldsymbol{x}), \tag{1c}$$

where $\boldsymbol{u} = (u, v, w)$ denotes the three-dimensional velocity field with streamwise component u, wall-normal component v and spanwise component w. The constant forcing in the streamwise direction is denoted by f_0 and $\boldsymbol{e}_1 = (1, 0, 0)$ is the unit vector in the streamwise direction. The boundary conditions are no-slip at the walls so that $\boldsymbol{u}(x, \pm\delta, z, t) = 0$, and periodic in the spanwise and streamwise directions. Here, the channel height in the wall-normal direction is 2δ.

C. Numerical experiment setup

The case we consider has a domain size of $\pi\delta \times 2\delta \times 0.34\pi\delta$ in the streamwise, wall-normal, and spanwise directions, respectively. The channel half-height δ was set to 1.0. The flow considered is at Reynolds number $\mathrm{Re} = 2200$ (corresponding to the friction Reynolds number $\mathrm{Re}_\tau = 110$) unless stated otherwise. The Reynolds number Re is defined as $\mathrm{Re} = \rho U\delta/\mu$ where ρ is the fluid density, U is the centerline velocity of a laminar flow with the same mass flow rate (as in Ref. [23]), and μ is the dynamic viscosity. As in Ref. [30], U was chosen so that the Mach number of the flow was under 0.3 and therefore the flow is nearly incompressible. Note that the Reynolds number corresponding to bulk velocity for this case is roughly 1500.

The friction Reynolds number Re_τ is defined as $\mathrm{Re}_\tau = \rho u_\tau \delta/\mu$ where $u_\tau = \sqrt{\tau_w/\rho}$ is the friction velocity and τ_w is the average shear stress at the wall. The channel constant forcing f_0 is set to balance the mean shear stress of the walls, so it is set by the choice of Reynolds number Re, and the friction Reynolds number Re_τ as follows:

$$f_0 = \frac{\tau_w}{\delta} = \frac{\mathrm{Re}_\tau^2}{\mathrm{Re}}\rho U. \tag{2}$$

The domain is discretized with a $4 \times 16 \times 2$ mesh with eighth-order spatial elements, resulting in a $32 \times 128 \times 16$ distribution of nodes (65 536 total), similar to the mesh used in Ref. [23]. The choice of $\mathrm{Re}_\tau = 110.0$ results in grid resolutions of $\Delta x^+ \approx 11$ and $\Delta z^+ \approx 7$ wall units per node, where $x^+ = u_\tau x/\nu$, $y^+ = u_\tau y/\nu$, and $z^+ = u_\tau z/\nu$.

The wall-normal spacing corresponds to $\Delta y^+ \approx 0.6$ for the nodes closest to the walls, which ensures that the simulations are well resolved. We used space-time elements that were 4th order in time and the time slab (temporal element) was $\Delta t = 0.05 t_e$, where $t_e = \delta/U$ denotes the eddy turnover time, the timescale associated with the largest possible eddy in the channel.

The DGSEM flow solver used here has been validated for the minimal flow unit at $\mathrm{Re} = 3000$ (equivalent to bulk velocity Reynold number of 2000) [30] and we carried out a similar validation study for the $\mathrm{Re} = 2200$ case. Note that the statistics at $\mathrm{Re} = 2200$ were only computed over time intervals when both walls had turbulent flow, as was done in Ref. [23] for low Reynolds number cases. This was necessary because the $\mathrm{Re} = 2200$ flow exhibited intermittent behavior similar to that observed in previous studies of minimal flow units.

D. Extreme events

The intermittent behavior of the flow at $\mathrm{Re} = 2200$ can be seen in Fig. 1 from the spikes in kinetic energy $E(t)$ and dissipation $Z(t)$. We define the kinetic energy,

$$E(t) = \iiint_\Omega \rho \boldsymbol{u} \cdot \boldsymbol{u}\, dx\, dy\, dz, \tag{3}$$

where Ω is the flow domain. Note that this is the total kinetic energy, comprised of both the mean and turbulent kinetic energy of the flow. Energy dissipation rate $Z(t)$ is defined as

$$Z(t) = \iiint_\Omega \mathrm{tr}(\boldsymbol{\tau}\nabla\boldsymbol{u})\, dx\, dy\, dz, \tag{4}$$

where $\boldsymbol{\tau}$ denotes the stress tensor, defined as $\boldsymbol{\tau} = \mu(\nabla\boldsymbol{u} + \nabla\boldsymbol{u}^\top)$ for an incompressible flow.

Figure 1 shows that large increases in $E(t)$ are followed by spikes in $Z(t)$ and a subsequent decrease in $E(t)$. These large spikes in kinetic energy occur when there is laminar flow near one wall, and nearly laminar flow near the other wall. Laminar flows correspond to higher kinetic energy $E(t)$ because the channel is driven by a constant body force in the axial direction. This body force acts as a fixed axial pressure gradient. The body force and wall shear stress balance one another when the flow is in an equilibrium state where we have

$$\mu\frac{\partial \overline{u}}{\partial n} = \delta\frac{\partial \overline{p}}{\partial x}, \tag{5}$$

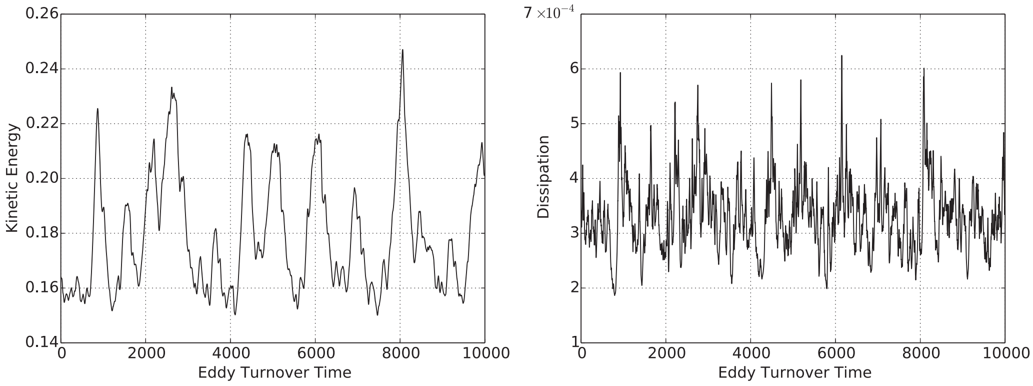

(a) (b)

FIG. 1. Time evolution of the kinetic energy (a) and the energy dissipation rate (b) for the near-wall minimal flow unit at Re = 2200.

where n is the wall-normal direction. For a given centerline velocity, a laminar flow will exert less shear stress $\mu\frac{\partial\bar{u}}{\partial n}$ on the walls than a turbulent flow, so for a given wall shear stress $\mu\frac{\partial\bar{u}}{\partial n}$ the laminar flow will have a larger centerline velocity than a turbulent flow.

Therefore, the large spikes in $E(t)$ are the result of a flow laminarization event. Of course, the flow never completely reaches the laminar state, though it gets very close it. Figures 2 and 3 show an example of a typical laminarization event where the flow undergoes the following stages:

(1) The flow on the bottom wall becomes laminar [Fig. 3(b)].

(2) The flow on the top wall becomes nearly laminar [Fig. 3(c)].

(3) As the entire channel becomes nearly laminar, the axial velocity increases.

(4) The higher velocities make the effective Reynolds number of the flow larger. This increases the likelihood of turbulent burst occuring since the flow is less stable to perturbations at a larger Reynolds number.

(5) A turbulent burst occurs on the top wall, which causes $Z(t)$ to increase rapidly [Fig. 3(d)].

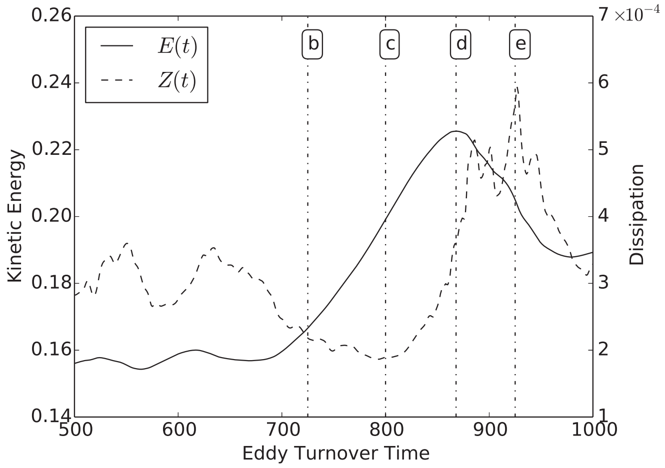

FIG. 2. Time evolution of $E(t)$ and $Z(t)$ during the first laminarization event shown in Fig. 1. The vertical lines indicate the times that snapshots in Fig. 3 correspond to. The first and last snapshot correspond to the start and end of the time horizon shown above.

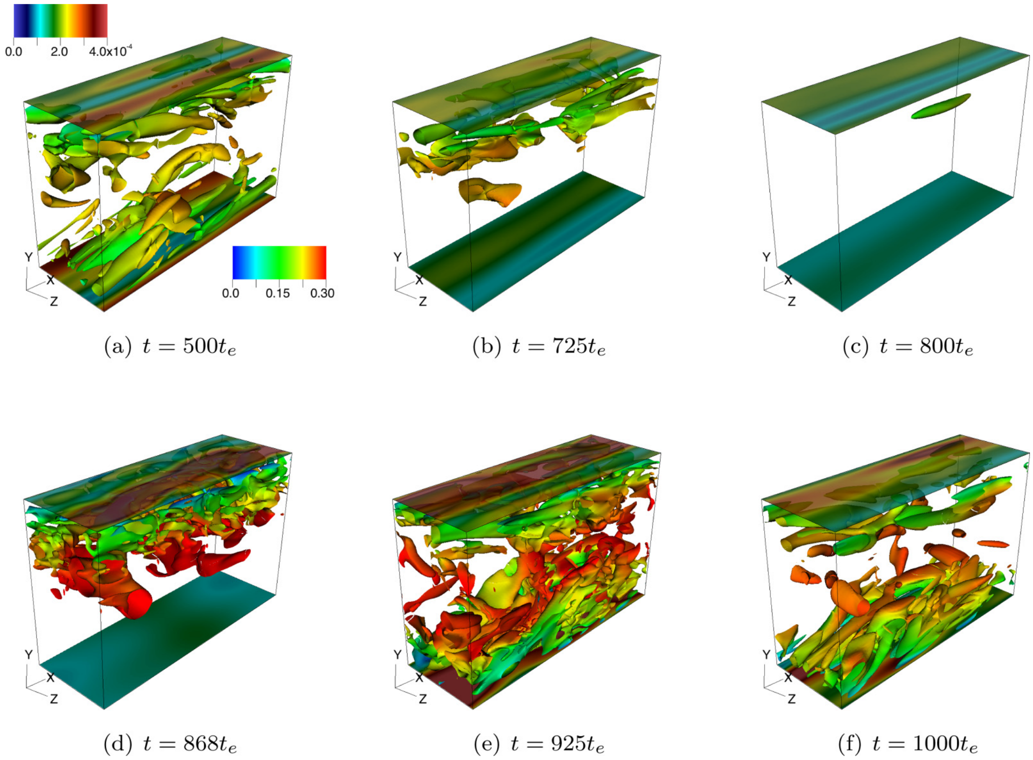

(a) $t = 500t_e$ (b) $t = 725t_e$ (c) $t = 800t_e$

(d) $t = 868t_e$ (e) $t = 925t_e$ (f) $t = 1000t_e$

FIG. 3. Snaphots of Q-criterion colored by axial velocity and wall shear stress. The axial velocity lies in the interval [0,0.3] and the wall shear stress lies in $[0, 4 \times 10^{-4}]$.

(6) The bottom wall transitions to turbulence [Fig. 3(e)].

(7) The turbulent flow on both walls causes $E(t)$ to decrease as it returns to the equilibrium mean turbulent flow profile [Fig. 3(f)].

These flow laminarization events, and the resulting bursts of energy dissipation rate, are the extreme events we will consider in this paper.

III. OPTIMAL STATES FOR EXTREME EVENTS

We now describe the constrained optimization problem whose solutions determine the most likely triggers of extreme events. The method is presented in detail in Ref. [3] and is reviewed here for completeness. We describe the optimization problem in the context of the channel flow, outline the numerical method for obtaining its solutions and present our numerical results.

A. High-likelihood triggers of extreme events

We seek initial states $\boldsymbol{u}_0$ that after a given integration time τ realize the largest possible energy growth. More precisely, we seek initial states $\boldsymbol{u}_0$ such that $E[\boldsymbol{u}(\tau)] - E(\boldsymbol{u}_0)$ is maximized. This is a PDE-constrained optimization problem, since the velocity field $\boldsymbol{u}(t)$ is required to satisfy the channel flow Eq. (1).

In addition to this PDE constraint, we also enforce a feasibility constraint, by requiring the initial state $\boldsymbol{u}_0$ to belong to the system attractor. This second constraint is essential to guarantee that the optimal solution is probabilistically relevant. As in many dissipative PDEs, the channel flow has an attractor towards which the solutions converge asymptotically after an initial transient. We are interested in the self-sustained and recurrent extreme events on this attractor as opposed to transient extreme events off the attractor that may occur but are not recurrent. To prevent the optimizer from considering such transient events, we enforce a feasibility constraint which is further elucidated in Sec. III B.

With this prelude, the optimization problem can be formulated as

$$\max_{\boldsymbol{u}_0\in\mathcal{U}}\{E[\boldsymbol{u}(\tau)]-E(\boldsymbol{u}_0)\}, \tag{6a}$$

$$\boldsymbol{u}(\tau) \text{ satisfies Eq. (1) with } \boldsymbol{u}(0)=\boldsymbol{u}_0, \tag{6b}$$

$$\boldsymbol{u}_0\in\mathcal{A}\subset\mathcal{U}, \tag{6c}$$

where $\tau > 0$ is a prescribed time, related to the growth timescale of a typical extreme event. The constraint Eq. (6b) implies that $\boldsymbol{u}(\tau)$ is a solution of the channel flow. Constraint Eq. (6c) ensures that the optimizer belongs to the attractor $\mathcal{A}$ and is therefore probabilistically relevant. Here, $\mathcal{U}$ denotes some appropriate function space. In the next section, we describe the method used to approximate the attractor $\mathcal{A}$.

B. Feasibility constraint and proper orthogonal decomposition

The attractors of dissipative dynamical systems are often very complex sets. Their estimation has been the subject of many studies (see, e.g., Ref. [40]). Here, we approximate the attractors via proper orthogonal decomposition (POD) of long-term simulations of the channel flow (this method is also known as the principal component analysis). The POD approximation assumes that the attractor has a Gaussian distribution with mean $\overline{\boldsymbol{u}}(\boldsymbol{x})$ and covariance matrix $\boldsymbol{C}(\boldsymbol{x},\boldsymbol{x}')$, where

$$\overline{\boldsymbol{u}}(\boldsymbol{x}) = \lim_{T\to\infty}\frac{1}{T}\int_0^T \boldsymbol{u}(\boldsymbol{x},t)dt, \tag{7a}$$

$$\boldsymbol{C}(\boldsymbol{x},\boldsymbol{x}') = \lim_{T\to\infty}\frac{1}{T}\int_0^T [\boldsymbol{u}(\boldsymbol{x},t)-\overline{\boldsymbol{u}}(\boldsymbol{x})]\otimes\big[\boldsymbol{u}(\boldsymbol{x}',t)-\overline{\boldsymbol{u}}(\boldsymbol{x}')\big]dt. \tag{7b}$$

Let the vector fields $\boldsymbol{v}_i : \Omega \to \mathbb{R}^3$ denote the eigenfunctions of the covariance tensor, so that

$$\int_\Omega \boldsymbol{C}(\boldsymbol{x},\boldsymbol{x}')\boldsymbol{v}_i(\boldsymbol{x}')d\boldsymbol{x}' = \lambda_i\boldsymbol{v}_i(\boldsymbol{x}), \quad i\in\mathbb{N}, \tag{8}$$

where $\lambda_i \in \mathbb{R}$ are the corresponding eigenvalues. The eigenvectors are ordered such that $\lambda_1 \geqslant \lambda_2 \geqslant \cdots$. Since the covariance tensor is symmetric and positive definite, the eigenvalues are real-valued and nonnegative, and furthermore the eigenfunctions are orthogonal with respect to the L^2 inner product, i.e., $\langle\boldsymbol{v}_i, \boldsymbol{v}_j\rangle_{L^2(\Omega)} = \delta_{ij}$. We refer to the eigenfunctions $\boldsymbol{v}_i$ as the POD modes.

In the POD approximation, any state on the attractor is approximated as

$$\boldsymbol{u}(\boldsymbol{x},t) = \overline{\boldsymbol{u}}(\boldsymbol{x}) + \sum_{i=1}^{n}\xi_i(t)\boldsymbol{v}_i(\boldsymbol{x}), \tag{9}$$

which is a finite-dimensional truncation to the first n POD modes. Each component of the vector $\boldsymbol{\xi} = (\xi_1, \cdots, \xi_n) \in \mathbb{R}^n$ is given by $\xi_i(t) = \langle\boldsymbol{u}(t) - \overline{\boldsymbol{u}}, \boldsymbol{v}_i\rangle_{L^2(\Omega)}$.

With this POD approximation of the attractor, the optimization problem Eq. (6) can be written more explicitly as

$$\max_{\boldsymbol{\xi}\in\mathbb{R}^n}\{E[\boldsymbol{u}(\tau)]-E(\boldsymbol{u}_0)\}, \tag{10a}$$

$$\boldsymbol{u}(\boldsymbol{x},\tau) \text{ satisfies Eq. (1) with } \boldsymbol{u}(\boldsymbol{x},0)=\boldsymbol{u}_0(\boldsymbol{x}), \tag{10b}$$

$$\boldsymbol{u}_0(\boldsymbol{x}) = \overline{\boldsymbol{u}}(\boldsymbol{x}) + \sum_{i=1}^{n}\xi_i\boldsymbol{v}_i(\boldsymbol{x}), \tag{10c}$$

$$\sum_{i=1}^{n}\frac{\xi_i^2}{\lambda_i} \leqslant r_0^2, \tag{10d}$$

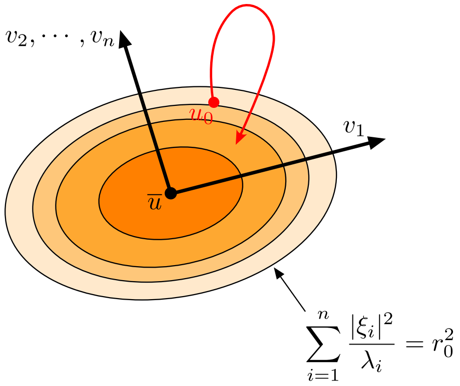

FIG. 4. A sketch of the proper orthogonal decomposition of the turbulent data. The attractor is approximated as an ellipsoid in the subspace spanned by the POD modes $\{\boldsymbol{v}_1, \cdots, \boldsymbol{v}_n\}$. The origin is the mean flow $\overline{\boldsymbol{u}}$.

where $r_0 \in \mathbb{R}$ is a prescribed parameter that is set equal to 1.0 in this study. Note that the form of the constraint essentially restricts our optimization within states that have the highest probability, given second-order statistics for the attractor. Constraint Eq. (10c) enforces that the mean-zero initial condition $\boldsymbol{u}_0 - \overline{\boldsymbol{u}}$ belongs to the subspace spanned by the first n POD modes. Constraint Eq. (10d), which describes an ellipsoid in the subspace span$\{\boldsymbol{v}_1, \cdots, \boldsymbol{v}_n\}$, ensures that the initial conditions are not two far from the mean flow $\overline{\boldsymbol{u}}$ (see Fig. 4).

Although the initial condition $\boldsymbol{u}_0$ is constrained to the subspace spanned by the first n POD modes, the final state $\boldsymbol{u}(\tau)$ may not belong to this subspace. This is because the POD decomposition is only an approximation of the attractor, which represents initial states for our analysis, and not the exact invariant attractor. However, we take n large enough so that only an insignificant fraction of the energy content of the states on the attractor are neglected. More precisely, in the following, we set $n = 50$ so that the truncation of the turbulent states to these POD modes contain at least 90% of the kinetic energy, as shown in Fig. 5.

As discussed in Sec. II D, previous studies of the minimal flow unit have shown that intermittent bursts of the flow originate from the near-wall activities. In light of these observations, we modify

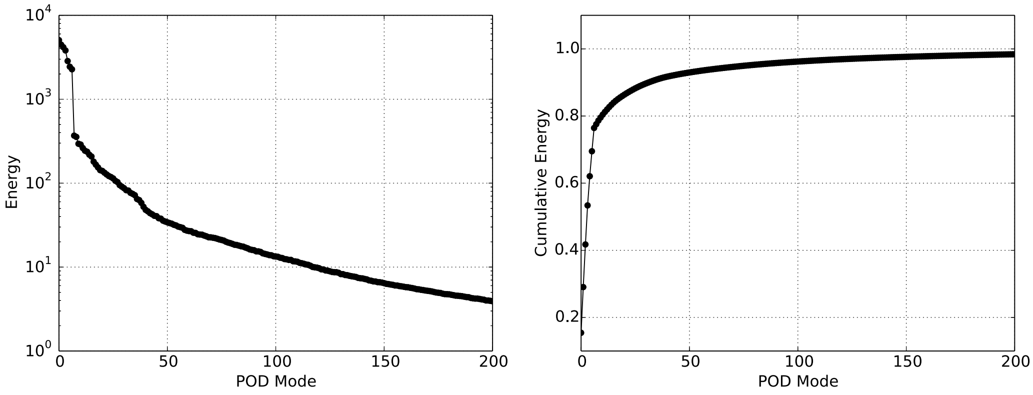

(a)

(b)

FIG. 5. The energy content of the POD modes. (a) Energy content of each POD mode. (b) Cumulative energy content of the POD modes. POD was computed with 1000 snapshots at Re = 2200.

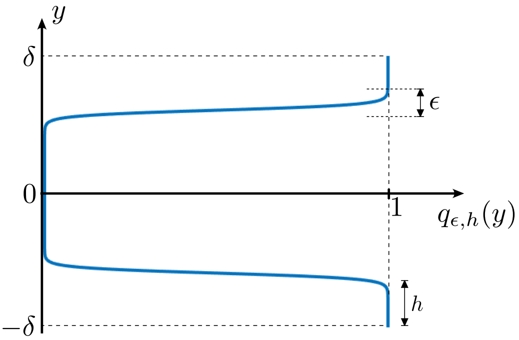

FIG. 6. A sketch of the weight function $q_{\epsilon,h}$ defined in Eq. (12).

the computation of the POD modes by multiplying the zero-mean velocity fields by a weight function that emphasizes the near-wall contribution of the flow. More precisely, we compute the weighted velocity fields,

$$\boldsymbol{u}_{\epsilon,h}(\boldsymbol{x},t) = [\boldsymbol{u}(\boldsymbol{x},t) - \overline{\boldsymbol{u}}(\boldsymbol{x})]q_{\epsilon,h}(y), \tag{11}$$

by multiply the original velocity fields $\boldsymbol{u}$ (after removing the mean $\overline{\boldsymbol{u}}$) with the weight function

$$q_{\epsilon,h}(y) = \frac{1}{2}\left(2 + \tanh\left\{\frac{1}{\epsilon}[y-(\delta-h)]\right\} - \tanh\left\{\frac{1}{\epsilon}[y+(\delta-h)]\right\}\right). \tag{12}$$

For $\epsilon \ll h \ll \delta$, the weight function $q_{\epsilon,h}$ vanishes near the center of the channel and approaches unity near the walls at $y = \pm\delta$ (see Fig. 6). The parameter h is the width of the near-wall region that we would like to emphasize and the small parameter ϵ determines how quickly the function $q_{\epsilon,h}$ decays to zero far from the walls.

We note that the weighting Eq. (11) is a linear operation on the velocity field, $\mathcal{L}(\boldsymbol{u}-\overline{\boldsymbol{u}}) := (\boldsymbol{u}-\overline{\boldsymbol{u}})q_{\epsilon,h}$, where the linear operator $\mathcal{L}$ is the multiplication by the weight $q_{\epsilon,h}$. It is straightforward to verify that $\mathcal{L}$ is a self-adjoint operator with respect to the $L^2(\Omega)$ inner product so that $\langle\mathcal{L}(\boldsymbol{u}_1-\overline{\boldsymbol{u}}),\mathcal{L}(\boldsymbol{u}_2-\overline{\boldsymbol{u}})\rangle_{L^2} = \langle(\boldsymbol{u}_1-\overline{\boldsymbol{u}}),\mathcal{L}^2(\boldsymbol{u}_2-\overline{\boldsymbol{u}})\rangle_{L^2}$ for all square integrable functions $\boldsymbol{u}_1,\boldsymbol{u}_2 \in L^2(\Omega)$. Therefore, introducing the weight function Eq. (11) is equivalent to replacing the L^2 inner product $\langle\cdot,\cdot\rangle_{L^2}$ with "weighted" inner product $\langle\cdot,\mathcal{L}^2\,\cdot\rangle_{L^2}$.

In practice, the POD modes are computed through the Eqs. (7) and (8) except that in computing the covariance Eq. (7b) instead of the terms $\boldsymbol{u}(\boldsymbol{x},t)-\overline{\boldsymbol{u}}(\boldsymbol{x})$, we use the mean-zero weighted velocity $\boldsymbol{u}_{\epsilon,h}(\boldsymbol{x},t)$. In the following, we set $\epsilon = 0.1$ to keep the decay smooth. We selected $h = 25\delta/110$ to emphasize the near-wall flow up to ignore any flow above $y^+ \approx 50$, where the minimal flow unit does not capture all length scales. This modified POD not only emphasizes the near-wall contributions, but also speeds up the convergence of the numerical optimization of problem Eq. (10).

The POD modes were computed using 1000 snapshots taken from flows computed from 10 different randomly chosen, initial conditions. The snapshots were taken at intervals of 50 eddy turnover times to minimize any correlation in time. Figure 5 shows the energy and cumulative energy of the POD modes. Almost 80% of the energy is captured by the first six modes, indicating that near-wall dynamics emphasized by our weight function are low dimensional.

Figure 7 shows a few of these modes. The shape of the most energetic modes is dominated by long axial streaks which are known to be a main feature of the near-wall region [31]. The more energetic modes such as modes 1 and 3 contain wider streaks, while less energetic modes such as mode 11 contain thinner, less coherent streaks that meander slightly.

Finally, we point out that an energy-maximizing optimization similar to Eq. (6) was used in Ref. [22] in the context of subcritical transition to turbulence from the laminar state in the pipe flow. It is important to emphasize that the problem of extreme events discussed here is different from the

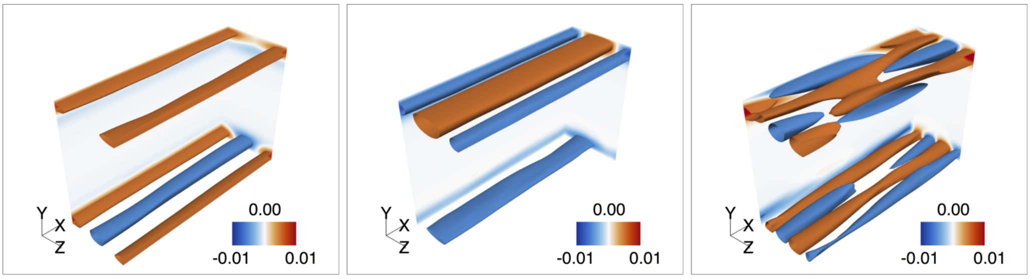

(a) Mode 1 (b) Mode 3 (c) Mode 11

FIG. 7. Contours and isosurfaces of axial velocity u for several POD modes. Isosurfaces are defined at $u = \pm 0.01$. Mode indicies are defined as in Fig. 5.

subcritical transition to turbulence. Specifically, despite the formal similarities to the constrained optimization presented in Ref. [22], the optimal states relevant to extreme events are not lying in small neighborhoods around the laminar state. In fact, we do not utilize the existence of a laminar state, since we employ information for the full turbulent attractor, in contrast to Ref. [22] where all the analysis is formulated around the laminar state. The present study demands that the initial states belong to the turbulent attractor as enforced through the constraint Eq. (6c) and implemented numerically in this section. In particular, our constraint is a hyper-ellipsoid around the statistical mean $\bar{\boldsymbol{u}}$ [see Eqs. (10c) and (10d)]. This set is not necessarily small and its extent is dictated by the flow dynamics (i.e., the eigenvalues λ_i of the covariance matrix).

Similarly, Farano *et al.* [41] investigated the observed bursts in a turbulent flow similar to our channel flow. However, they only require that the energy of the optimal state is prescribed, i.e., $E(\boldsymbol{u}_0) = E_0$ for a prescribed energy level E_0. This does not necessarily imply that the optimal state belongs to the attractor and therefore unphysical optimizers are not ruled out.

C. Numerical implementation

The optimization problem, Eq. (10), was solved using the Python package scipy [42]. Specifically, the "optimize" package was used and the optimization was carried out using sequential least squares programming (SLSQP). The first constraint, Eq. (10b), is implicitly satisfied by the flow solver, which is called from Python using the "multiprocessing" module. The second and third constraint Eqs. (10c) and (10d) and their gradients are implemented directly in Python. The convergence tolerance for the objective function was set to 10^{-7}. Otherwise, the default convergence criterion were used. An adjoint solver was used to minimize the cost of computing the gradient of the objective function Eq. (10a). The DGSEM solver has a dual consistent, discrete adjoint formulation, details of which are discussed in Refs. [33,37]. This adjoint solver allows us to compute the gradient at a computational cost similar to solving the primal, which is much cheaper than using finite differences to compute the gradient with respect to all $n = 50$ POD modes.

Since we use a gradient-based optimization, SLSQP seeks the local optimizers. Since the problem is highly nonconvex, we are unaware of optimization methods that can provably guarantee the convergence to the global optimizer. Therefore, we run the SLSQP algorithm from several initial guesses $\boldsymbol{u}_0$ in the constraint set $\mathcal{A}$ and retain the local optimizer that corresponds to the largest energy growth among them.

D. Optimization results

The optimization was run from five different initial guesses $\boldsymbol{u}_0$ and with three different integration times of $\tau = 52.5t_e$, $\tau = 105t_e$, and $\tau = 210t_e$. The integration times correspond to roughly 1/8, 1/4, and 1/2 of the timescale of laminarization event similar to the one shown in Fig. 2. All five

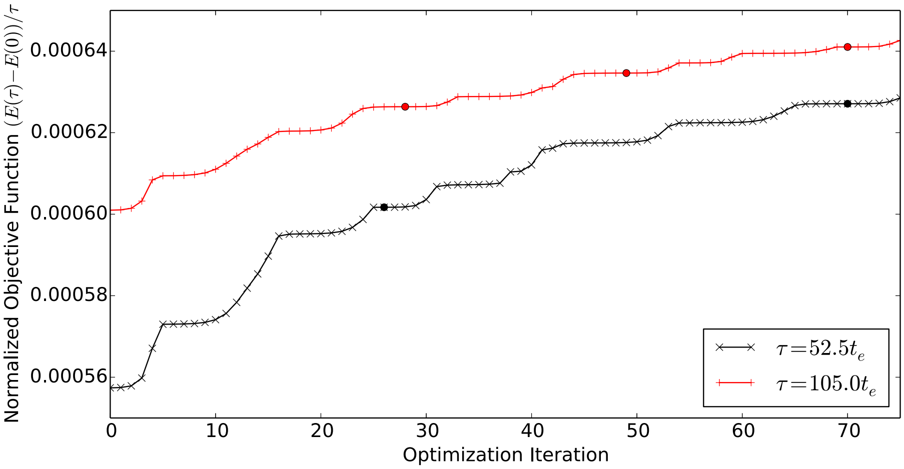

FIG. 8. Convergence of the objective function for the same initial guess but two different choices of τ. Solid dots represent instances when the optimizer was restarted.

optimizations with $\tau = 52.5t_e$ and $\tau = 105t_e$ computed very similar optimal solutions $\boldsymbol{u}_0^*$. All these optimizers belong to the interior of the constraint set (10d), i.e., they satisfy $\sum_i \xi_i^2/\lambda_i < 1$. This does not imply that the constraint was not employed. On the contrary, the constraint was utilized during the optimization process to prevent the convergence to an optimal solution outside the constraint set. The optimization with an integration time of $\tau = 210t_e$ failed to converge because the adjoint grew very large in magnitude, and the gradient caused the optimizer to consider a nonphysical solution in the ensuing line search.

Figure 8 shows the convergence history of a typical optimization for $\tau = 52.5t_e$. The corresponding POD mode weights for the initial guess and optimal solution are shown in Fig. 9. The two largest POD modes in the optimal solution are modes 6 and 26, shown in Fig. 10. Together, these modes create the axial velocity deficit in the near wall region shown in Fig. 11. The maximum velocity deficit occurs roughly $y^+ = 18$ units from each wall, and decays to zero roughly $y^+ \approx 55$ units from the wall.

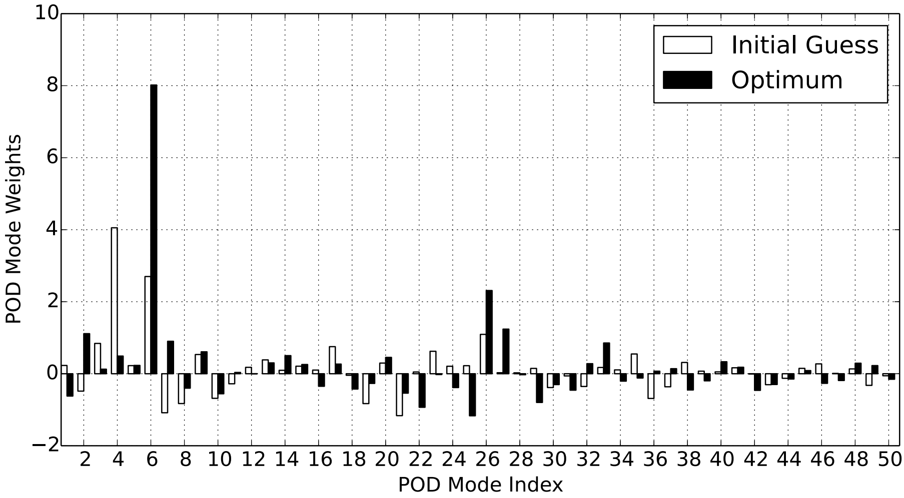

FIG. 9. POD mode weights for the initial guess and optimal solution.

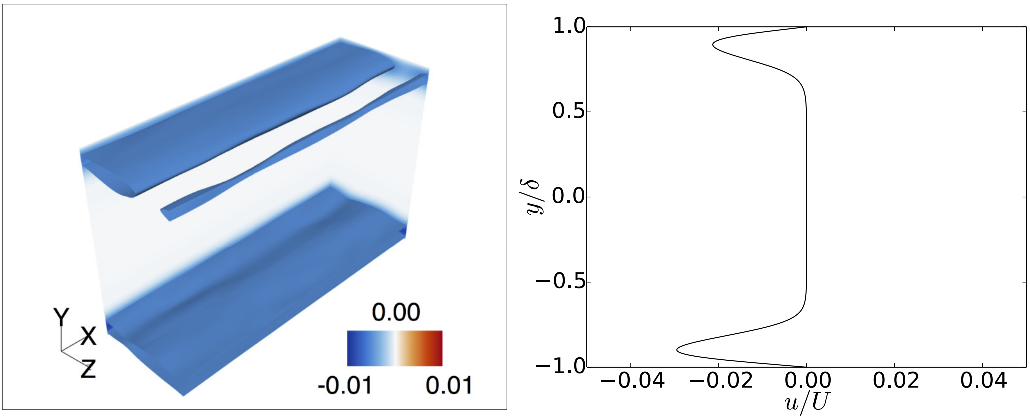

(a) Mode 6 (b) Mode 6 Profile

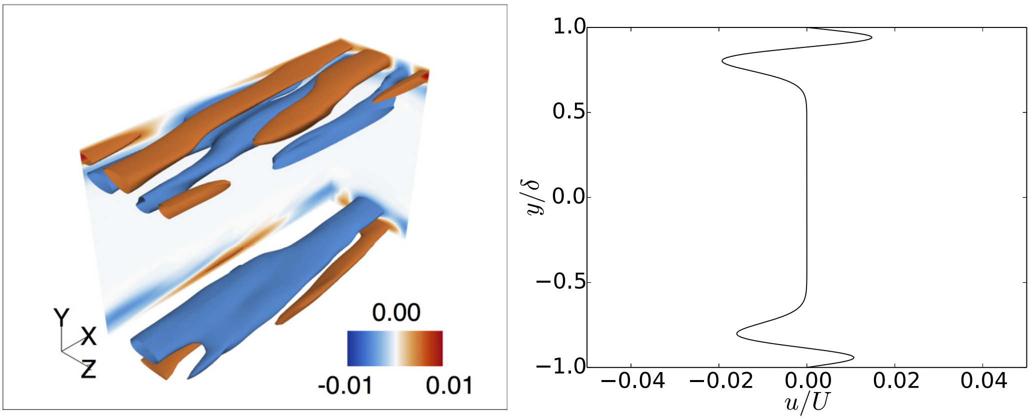

(c) Mode 26 (d) Mode 26 Profile

FIG. 10. Contours, isosurfaces, and spatially averaged profiles of axial velocity for the two most energetic POD modes in the optimal solution to Eq. (10). Isosurfaces are defined at $u \pm 0.01$.

The region in which the velocity deficit occurs is known to have a major impact on near-wall turbulence. In Ref. [26] it was observed that damping axial velocity streaks or quasistreamwise vortex structures between $y^+ \approx 20$ to $y^+ \approx 60$ led to laminarization of the near wall region. It appears that our optimal solution modifies the lower portion of this range. The relative uniformity of the axial velocity deficit results in the absence of axial velocity streaks and quasistreamwise vortex structures. This is in contrast with the flow snapshots in Fig. 3, where the presence of low- and high-axial velocity streaks can be inferred from streaks in the wall shear stress, and quasiaxial structures are revealed by the q-criterion isocontours. Without the axial velocity streaks and quasistreamwise vorticity, the “streak-cycle” mechanism for the regeneration of near-wall turbulent fluctuations is broken and the flow laminarizes.

Therefore, although the optimal solution $\boldsymbol{u}_0^*$ is turbulent, the absence of axial velocity streaks and quasistreamwise vortices make it a precursor for a flow laminarization. By tracking how close a given state is to $\boldsymbol{u}_0^*$, we can determine if a laminarization event is likely to occur or not.

Although we can compute the precursor for the relatively low Reynolds number flows considered in this paper, the adjoint growth issue encountered for $\tau = 210t_e$ suggests that this approach will

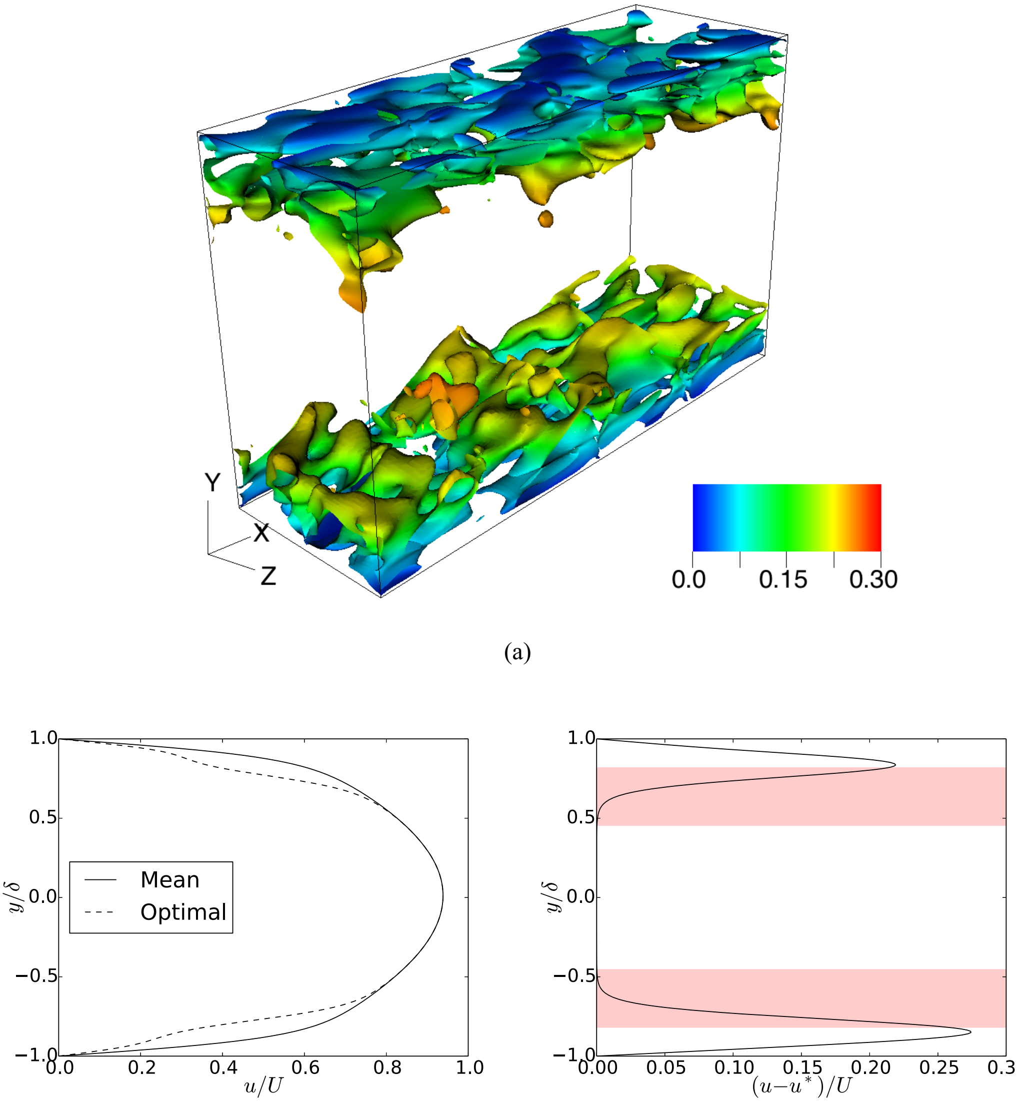

(a)

(b)

(c)

FIG. 11. Optimal solution $\boldsymbol{u}_0^*$ to Eq. (10). (a) Q criterion isosurface for $Q = 0.0005$, colored by the streamwise velocity (b) Spatially averaged streamwise velocity profile with the mean axial velocity profile. (c) Spatially averaged streamwise velocity profile difference. Red-shaded boxes indicate regions from $y^+ = 20$ to $y^+ = 60$ units away from the wall.

not scale well with Reynolds number. The adjoint grows exponentially in time at a rate roughly equal to the largest Lyapunov exponent of the flow [43]. The maximum Lyapunov exponent grows in turn as the Reynolds number increases [44]. As a result, computing the optimal solution at higher Reynolds numbers by a straightforward adjoint optimization may face numerical instability issues. Approaches like least squares shadowing have been shown to eliminate exponential growth of the adjoint for time-averaged objective functions [45], but to the authors' knowledge no such approach exists for transient objective functions like that in our optimization problem Eq. (6).

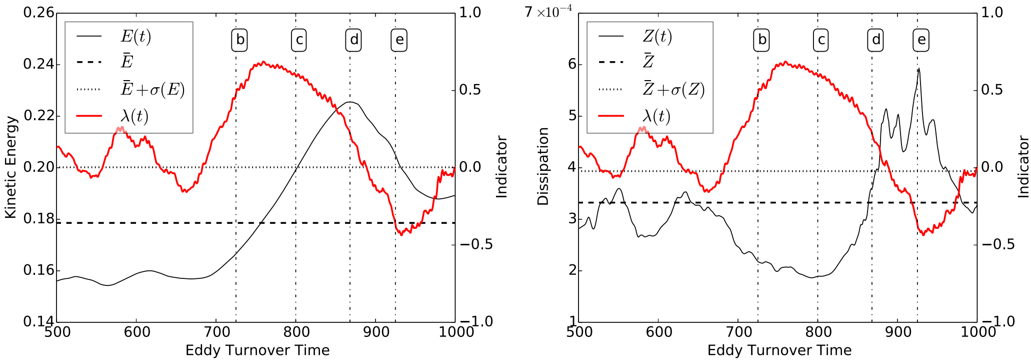

(a)

(b)

FIG. 12. Time evolution of the indicator $\lambda(t)$ with $E(t)$ and $Z(t)$ over the same time horizon as shown in Fig. 2. The horizontal lines indicate the mean ($\bar{X}$) and the mean plus one standard deviation $[\bar{X} + \sigma(X)]$ of $E(t)$ and $Z(t)$. The vertical lines indicate the times that snapshots in Fig. 3 correspond to. The first and last snapshot correspond to the start and end of the time horizon shown above.

IV. PREDICTING EXTREME EVENTS

Figure 12 shows a close-up of the evolution of energy E and dissipation Z together with the indicator

$$\lambda = \frac{\langle \boldsymbol{u} - \bar{\boldsymbol{u}}, \boldsymbol{u}_0^* - \bar{\boldsymbol{u}} \rangle}{\|\boldsymbol{u} - \bar{\boldsymbol{u}}\|_2 \|\boldsymbol{u}_0^* - \bar{\boldsymbol{u}}\|_2}, \tag{13}$$

at Re = 2200. Large values of energy and dissipation are proceeded with relatively large values of the indicator. This behavior turns out to be generic and not specific to this time window. As a result, one can use the indicator λ to predict the upcoming extreme events in the channel flow. To quantify these predictions, we first review some statistical tools in Sec. IV A. Subsequently, in Sec. IV B, we apply these tools to long-term simulations of the channel flow and report the results.

A. Statistical preliminaries

In this section, we show that the trigger state obtained previously can be used for the prediction of the extreme events in the channel flow. To make quantitative statements, we use joint and conditional statistics between the trigger mode and the energetic observables of the turbulent flow, namely, kinetic energy and energy dissipation rate.

For a given random variable X_t, we would like to find an indicator Y_t (another random variable) whose values signal an upcoming extreme event of X_t. We identify extreme events of X_t as any instant where $X_t > x_e$ for a prescribed extreme value threshold x_e. First, we define the maximum value of the random variable X_t over a future time interval $[t + t_0, t + t_0 + \Delta t]$ for some t_0, $\Delta t \geqslant 0$,

$$\tilde{X}_t(t_0, \Delta t) = \max_{s \in [t+t_0, t+t_0+\Delta t]} X_s. \tag{14}$$

The maximum $\tilde{X}_t(t_0, \Delta t)$ is a new random variable which depends on the parameters t_0 and Δt. At any time t, $\tilde{X}_t(t_0, \Delta t)$ measures the maximum value that X_t will take over the future time interval $[t + t_0, t + t_0 + \Delta t]$. For notational simplicity, we omit the parameters t_0 and Δt and simply write $\tilde{X}_t$.

The joint probability distribution of the pair $(\tilde{X}_t, Y_t)$ is defined by

$$F_{\tilde{X}_t, Y_t}(x, y) = \mathbb{P}(\tilde{X}_t \leqslant x, Y_t \leqslant y) = \int_{-\infty}^{x} \int_{-\infty}^{y} p_{\tilde{X}_t, Y_t}(x, y) dx dy, \tag{15}$$

where $p_{\tilde{X}_t,Y_t}$ is the probability density associated with the probability distribution $F_{\tilde{X}_t,Y_t}$. Roughly speaking, the quantity $p_{\tilde{X}_t,Y_t}(x,y)dxdy$ measures the probability that at time t we observe $x < \tilde{X}_t < x + dx$ and $y < Y_t < y + dy$.

The conditional probability of $\tilde{X}_t = x$ given that $Y_t = y$ is defined through the Bayes' formula,

$$p_{\tilde{X}_t|Y_t} = \frac{p_{\tilde{X}_t,Y_t}}{p_{Y_t}}, \tag{16}$$

where p_{Y_t} is the probability density associated with the random variable Y_t. We use the conditional PDF $p_{\tilde{X}_t|Y_t}$ to quantify the extent to which the behavior of Y_t is indicative of the extreme events of X_t over the future time interval $[t + t_0, t + t_0 + \Delta t]$. More precisely, given an extreme event threshold x_e, we define the probability of upcoming extreme events by

$$P_{ee}(y) = \int_{x_e}^{\infty} p_{\tilde{X}_t|Y_t}(x,y)dx. \tag{17}$$

This quantity measures the probability of an extreme event over the future time interval $[t + t_0, t + t_0 + \Delta t]$ given the current value of the indicator $Y_t = y$.

For a reliable indicator, P_{ee} should be monotonic so that the probability of upcoming extreme events increases with y. More precisely, P_{ee} should be nearly zero for small values of y and increase monotonically towards 1 as y increases. We predict an upcoming extreme only if $P_{ee} > 0.5$. This defines an extreme event threshold y_e for the indicator Y_t where $P_{ee}(y_e) = 0.5$. If $Y_t > y_e$, then an upcoming extreme event is predicted, and conversely, if $Y_t < y_e$, then it is predicted that no extreme events will occur over the future time interval $[t + t_0, t + t_0 + \Delta t]$.

This classification leads to four possible prediction outcomes in terms of the indicator value Y_t and the future observable values $\tilde{X}_t$:

$$\begin{aligned} \text{Correct Rejection (CR):} \quad & \tilde{X}_t < x_e \quad \text{given} \quad Y_t < y_e, \\ \text{Correct Prediction (CP):} \quad & \tilde{X}_t > x_e \quad \text{given} \quad Y_t > y_e, \\ \text{False Negatives (FN):} \quad & \tilde{X}_t > x_e \quad \text{given} \quad Y_t < y_e, \\ \text{False Positive (FP):} \quad & \tilde{X}_t < x_e \quad \text{given} \quad Y_t > y_e. \end{aligned} \tag{18}$$

Therefore, the skill of an indicator for predicting upcoming extreme events can be quantifies as follows:

$$\text{Rate of successful predictions} = \frac{\text{CP}}{\text{CP} + \text{FN}} = \frac{\int_{x_e}^{\infty}\int_{y_e}^{\infty} p_{\tilde{X}_t|Y_t}(x,y)dydx}{\int_{x_e}^{\infty}\int_{-\infty}^{\infty} p_{\tilde{X}_t|Y_t}(x,y)dydx}, \tag{19a}$$

$$\text{Rate of successful rejections} = \frac{\text{CR}}{\text{CR} + \text{FP}} = \frac{\int_{-\infty}^{x_e}\int_{-\infty}^{y_e} p_{\tilde{X}_t|Y_t}(x,y)dydx}{\int_{-\infty}^{x_e}\int_{-\infty}^{\infty} p_{\tilde{X}_t|Y_t}(x,y)dydx}. \tag{19b}$$

A skillful indicator is one that returns relatively small percentage of false negatives (respectively, false positives) compared to the number of correct predictions (respectively, correct rejections). In the following, we use the statistical quantities introduced above to quantify the predictive skill of the indicator Eq. (13).

B. Prediction results

We first present the joint and conditional statistics for the energy E, dissipation rate Z and the indicator λ. In this first step, we do not include any time shifts, thus setting $t_0 = \Delta t = 0$ so that $\tilde{X}_t = X_t$ in Eq. (14). Figure 13 shows the joint and conditional PDFs of the indicator versus energy E

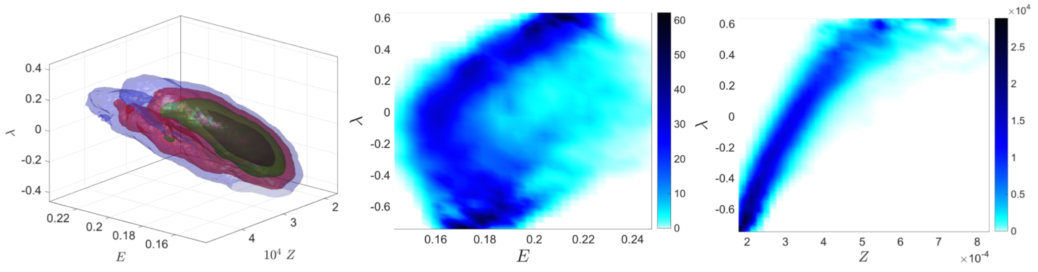

(a) (b) (c)

FIG. 13. Probability densities at Re $= 2200$. (a) Joint PDF of the kinetic energy E, energy dissipation Z and the indicator λ. (b) Conditional PDF $p_{E|\lambda}$. (c) Conditional PDF $p_{Z|\lambda}$.

and the energy dissipation Z at Re $= 2200$. This figure is generated from an ensemble of long-term simulations with data recorded every one eddy turnover time collecting a total of 106 063 data points.

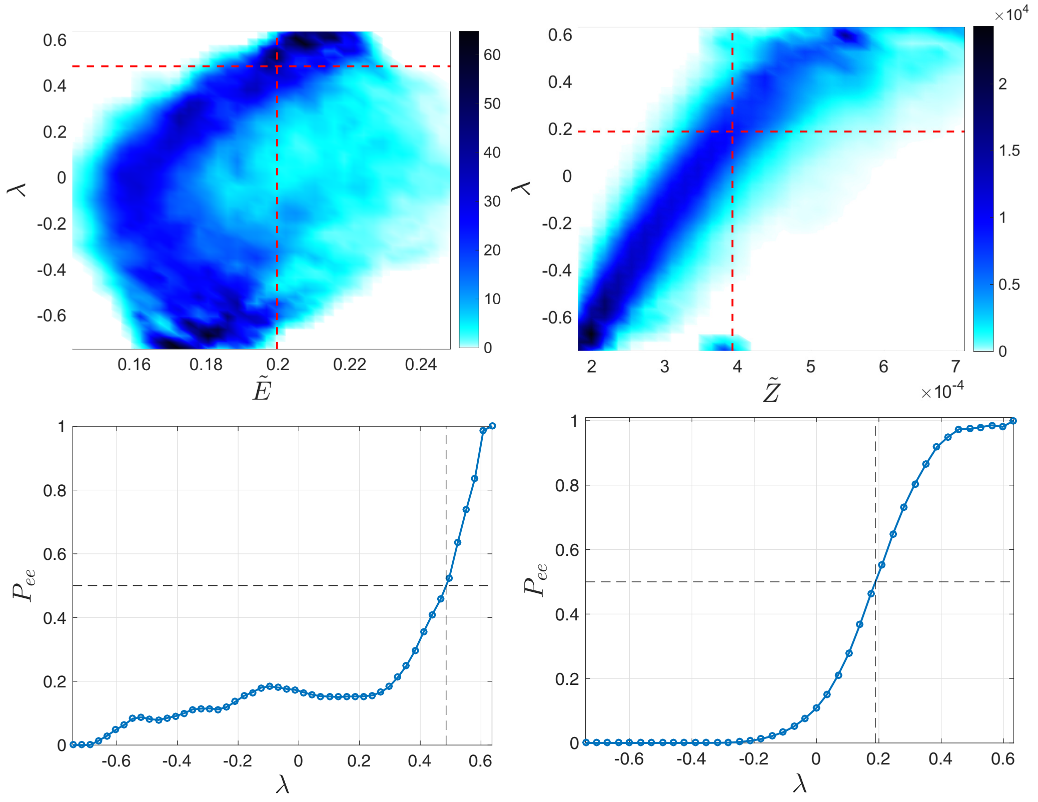

(a) (b)

FIG. 14. Predictive conditional probability densities. (a) Top row: Conditional PDF $p_{\tilde{E}|\lambda}$ computed with $t_0 = t_e$ and $\Delta t = 10 t_e$ where t_e denotes the eddy turnover time. The vertical dashed line marks the threshold E_e of extreme events that is prescribed as the mean of E plus one standard deviation. The horizontal dashed line marks the extreme event threshold λ_e according to the indicator λ. Bottom row: The probability of upcoming extreme events P_{ee}. The horizontal dashed line marks $P_{ee} = 0.5$ and the vertical dashed line marks the extreme event threshold λ_e so that $P_{ee}(\lambda_e) = 0.5$. (b) Same as panel (a) but the figure correspond to the energy dissipation Z versus the indicator λ.

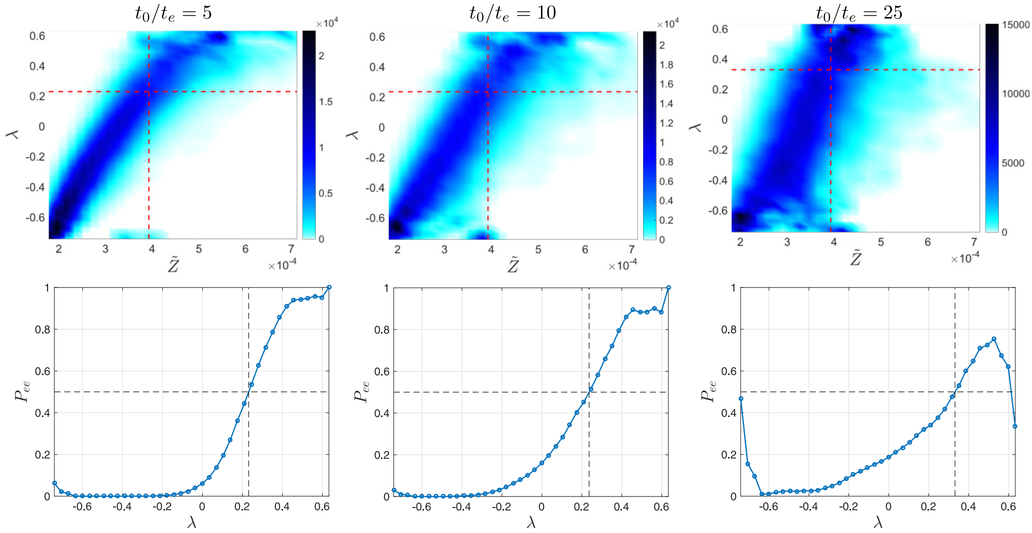

FIG. 15. Prediction quality for varying prediction times t_0. In all plots, the length of the future maximum time window in Eq. (14) is $\Delta t = 10$. First row shows the conditional PDF $p_{\tilde{Z}|\lambda}$ and the second row shows the corresponding probability of future extreme events defined in Eq. (17).

The shape of the conditional PDFs $p_{E|\lambda}$ and $p_{Z|\lambda}$ shows that the extreme values of the indicator λ correlate strongly with relatively large energy and large dissipation episodes [see Figs. 13(a) and 13(b)]. We also note that that the correlation is much stronger for dissipation and that λ tends to increase monotonically with the dissipation Z.

The next step is to introduce a time lag to investigate whether the large indicator values precede the extreme episodes of energy and dissipation. This is clearly the case in Fig. 12, where the peak of the indicator precedes the extreme values of energy (and energy dissipation) by about 50 to 100 eddy turnover times. Below we show that this is generally the case during the long-term simulations. We point out, however, that Fig. 12 depicts an unusual extreme event in that the prediction time t_0 is very long. On average the prediction times are much shorter (on the order of a few eddy turnover times).

Figure 14 shows the conditional PDFs $p_{\tilde{E}|\lambda}$ and $p_{\tilde{Z}|\lambda}$ where the future maxima $\tilde{E}$ and $\tilde{Z}$ are computed with $t_0 = t_e$ and $\Delta t = 10t_e$ [see Eq. (14)]. The extreme value threshold E_e (respectively, Z_e) are set as the mean of energy (respectively, dissipation) plus one standard deviation. Figure 14

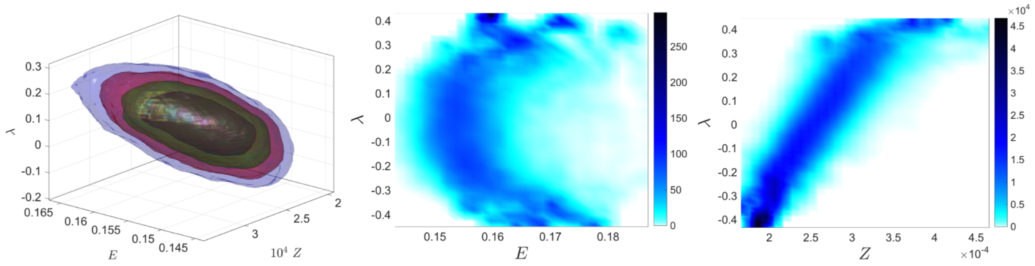

(a) (b) (c)

FIG. 16. Probability densities at Re = 3000. (a) Joint PDF of the kinetic energy E, energy dissipation Z and the indicator λ. (b) Conditional PDF of Y_t = Indicator and X_t = Energy. (c) Conditional PDF of Y_t = Indicator and X_t = Energy Dissipation.

TABLE I. The prediction skill of the indicator λ at two Reynolds numbers. The rate of successful rejections (RSR) and the rate of successful predictions (RSP) are reported for the energy dissipation rate Z. The parameters t_0 and Δt denote the prediction time parameters defined in Ref. (14).

Re	t_0/t_e	$\Delta t/t_e$	RSP	RSR
2200	1	10	86.9%	94.7%
	2	10	86.7%	94.3%
	3	10	86.4%	93.8%
3000	1	5	79.4%	91.7%
	2	5	75.4%	92.6%
	3	5	74.9%	92.2%

also shows the corresponding P_{ee} computed from Eq. (17). The extreme event threshold according to the indicator λ is the point at which $P_{ee}(\lambda_e) = 0.5$.

As the prediction time t_0 increases, we expect the prediction skill of the indicator to deteriorate. This is shown in Fig. 15 where the conditional PDF $p_{\tilde{Z}|\lambda}$ are shown for increasing prediction times t_0. For prediction times as large as $t_0 = 10t_e$ the prediction skill of the indicator is still reasonably satisfactory. However, as the prediction time increases to close $t_0 = 25t_e$ the predictor returns significant amount of false positives and false negatives, thus losing its predictive value. The rates of successful predictions and successful rejections, defined in Eq. (19), are reported in Table I for a few prediction time horizons.

Similar results are observed at higher Reynolds numbers. Figure 16 shows the joint and conditional PDFs of the indicator, energy and dissipation at Re = 3000. These PDFs resemble those of Fig. 13 for the lower Reynold number Re = 2200. This demonstrates clearly the robustness of the derived indicator. Table I also contains the rates of success in predicting extreme (and nonextreme) events at Re = 3000. We point out that the channel flow at some intermediate Reynolds numbers between Re = 2200 and Re = 3000 did not exhibit extreme events in the time horizons we simulated.

Finally, we recall that the predictability time of chaotic systems is inversely proportional to their leading Lyapunov exponent [46] because of the exponential growth of uncertainties (this holds for both extreme and nonextreme events). Therefore, the prediction of extreme events is fundamentally limited by the predictability time horizon set by the leading Lyapunov exponent. Since the Lyapunov exponent increases with the Reynolds number, we expect the prediction time t_0 to decrease at higher Reynolds flows.

V. CONCLUSIONS

We have demonstrated an original approach for the derivation of precursors of extreme events in a challenging problem involving a turbulent channel flow. The extreme events in this case have the form of random near-laminarization episodes that lead to bursts of the kinetic energy and the energy dissipation rate. We formulate a constrained optimization problem that searches for initial states with the most intense growth of kinetic energy, within a constrained set in the core of the underlying turbulent attractor. By searching over a high-probability set, we achieve a numerically tractable optimization problem, while at the same time we exclude exotic states that may correspond to intense growth of energy but have very low probability to occur if we are close to the attractor.

The derived precursor is demonstrated to successfully capture extreme dissipation episodes several eddy turnover times before the event. We have discussed its physical relevance and have demonstrated its robustness as the Reynolds number of the flow changes. Because the developed scheme utilizes the full nonlinear equations and not linearized approximations, it has the potential to be extended to more complex flows. However, one should exercise caution in using adjoint-based optimization at higher Reynolds numbers. As we mentioned in Sec. III D, the straightforward backward integration of the adjoint equation at high Reynolds numbers is often unstable and therefore alternative optimization methods should be considered.

Nonetheless, the success of the presented approach to an intermittently turbulent channel flow implies the potential of the method for studying transitional flows, such as bypass transition of boundary layers. Our future endeavors include the utilization of these precursors for the control and suppression of extreme events in these systems.

ACKNOWLEDGMENTS

T.P.S. and M.F. have been supported through the ARO MURI W911NF-17-1-0306 and the ONR Grant No. N00014-15-1-2381. P.J.B. was supported by an appointment to the NASA Postdoctoral Program at the NASA Ames Research Center, administered by Universities Space Research Association under contract with NASA. Specifically, the research efforts of P.J.B. were sponsored by NASA's Transformational Tools and Technologies (TTT) Project of the Transformative Aeronautics Concepts Program under the Aeronautics Research Mission Directorate. Resources supporting this work were provided by the NASA High-End Computing (HEC) Program through the NASA Advanced Supercomputing (NAS) Division at Ames Research Center. We are also grateful to the anonymous referees for their comments which improved the presentation of this paper.

[1] T. P. Sapsis and A. J. Majda, A statistically accurate modified quasilinear Gaussian closure for uncertainty quantification in turbulent dynamical systems, Physica D **252**, 34 (2013).

[2] T. P. Sapsis and A. J. Majda, Statistically accurate low-order models for uncertainty quantification in turbulent dynamical systems, Proc. Natl. Acad. Sci. USA **110**, 13705 (2013).

[3] M. Farazmand and T. P. Sapsis, A variational approach to probing extreme events in turbulent dynamical systems, Sci. Adv. **3**, e1701533 (2017).

[4] M. A. Mohamad, W. Cousins, and T. P. Sapsis, A probabilistic decomposition-synthesis method for the quantification of rare events due to internal instabilities, J. Comput. Phys. **322**, 288 (2016).

[5] M. A. Mohamad and T. P. Sapsis, Probabilistic description of extreme events in intermittently unstable dynamical systems excited by correlated stochastic processes, SIAM/ASA J. Uncert. Quant. **3**, 709 (2015).

[6] A. Majda, M. Moore, and D. Qi, Statistical dynamical model to predict extreme events and anomalous features in shallow water waves with abrupt depth change, Proc. Natl. Acad. Sci. **116**, 3982 (2019).

[7] D. Qi and A. Majda, Predicting extreme events for passive scalar turbulence in two-layer baroclinic flows through reduced-order stochastic models, Commun. Math. Sci. **16**, 17 (2018).

[8] J. Kim, P. Moin, and R. Moser, Turbulence statistics in fully developed channel flow at low Reynolds number, J. Fluid Mech. **177**, 133 (1986).

[9] N. Aubry, P. Holmes, J. Lumley, and E. Stone, The dynamics of coherent structures in the wall region of a turbulent boundary layer, J. Fluid Mech. **192**, 115 (1988).

[10] M. Farazmand, An adjoint-based approach for finding invariant solutions of Navier-Stokes equations, J. Fluid Mech. **795**, 278 (2016).

[11] M. Farazmand and T. P. Sapsis, Extreme Events: Mechanisms and Prediction, Appl. Mech. Rev. (2018), doi:10.1115/1.4042065.

[12] I. Mezić, Analysis of fluid flows via spectral properties of the Koopman operator, Annu. Rev. Fluid Mech. **45**, 357 (2013).

[13] C. W. Rowley, I. Mezić, S. Bagheri, P. Schlatter, and D. S. Henningson, Spectral analysis of nonlinear flows, J. Fluid Mech. **641**, 115 (2009).

[14] K. K. Chen, J. H. Tu, and C. W. Rowley, Variants of dynamic mode decomposition: boundary condition, Koopman, and Fourier analyses, J. Nonlin. Sci. **22**, 887 (2012).

[15] P. J. Schmid, Dynamic mode decomposition of numerical and experimental data, J. Fluid Mech. **656**, 5 (2010).

[16] M. O. Williams, I. G. Kevrekidis, and C. W. Rowley, A data–driven approximation of the Koopman operator: Extending dynamic mode decomposition, J. Nonlin. Sci. **25**, 1307 (2015).

[17] H. Babaee, M. Farazmand, G. Haller, and T. P. Sapsis, Reduced-order description of transient instabilities and computation of finite-time Lyapunov exponents, Chaos **27**, 063103 (2017).

[18] M. Farazmand and T. Sapsis, Dynamical indicators for the prediction of bursting phenomena in high-dimensional systems, Phys. Rev. E **94**, 032212 (2016).

[19] J. N. Kutz, Xi. Fu, and S. L. Brunton, Multiresolution dynamic mode decomposition, SIAM J. Appl. Dyn. Syst. **15**, 713 (2015).

[20] G. Dematteis, T. Grafke, and E. Vanden-Eijnden, Rogue waves and large deviations in deep sea, Proc. Natl. Acad. Sci. **115**, 855 (2018).

[21] T. P. Sapsis, New perspectives for the prediction and statistical quantification of extreme events in high-dimensional dynamical systems, Philos. Trans. R. Soc. London A **376**, 20170133 (2018).

[22] C. C. T. Pringle and R. R. Kerswell, Using Nonlinear Transient Growth to Construct the Minimal Seed for Shear Flow Turbulence, Phys. Rev. Lett. **105**, 154502 (2010).

[23] J. Jimenez and P. Moin, The minimal flow unit in near-wall turbulence, J. Fluid Mech. **225**, 213 (1991).

[24] H. A. Carlson and J. L. Lumley, Active control in the turbulent wall layer of a minimal flow unit, J. Fluid Mech. **329**, 341 (1996).

[25] O. Florez and J. Jimenez, Hierarchy of minimal flow units in the logarithmic layer, Phys. Fluids **22**, 071704 (2010).

[26] J. Jimenez and A. Pinelli, The autonomous cycle of near-wall turbulence, J. Fluid Mech. **389**, 335 (1999).

[27] J. Jimenez and M. P. Simens, Low-dimensional dynamics of a turbulent wall flow, J. Fluid Mech. **435**, 81 (2001).

[28] D. Chung, L. Chan, M. MacDonald, N. Hutchins, and A. Ooi, A fast direct numerical simulation method for characterizing hydraulic roughness, J. Fluid Mech. **773**, 418 (2015).

[29] M. MacDonald, D. Chung, N. Hutchins, L. Chan, A. Ooi, and R. Garcia-Mayoral, The minimal-span channel for rough-wall turbulent flows, J. Fluid Mech. **816**, 5 (2017).

[30] P. J. Blonigan, Adjoint sensitivity analysis of chaotic dynamical systems with non-intrusive least squares shadowing, J. Comput. Phys. **348**, 803 (2017).

[31] J. Jimenez, Cascades in wall-bounded turbulence, Annu. Rev. Fluid Mech. **44**, 27 (2012).

[32] J. Jiménez, Coherent structures in wall-bounded turbulence, J. Fluid Mech. **842**, P1 (2018).

[33] C. Carton de Wiart, L. T. Diosady, A. Garai, N. K. Burgess, P. J. Blonigan, D. Ekelschot, and S. M. Murman, Design of a modular monolithic implicit solver for multi-physics applications, in *Proceedings of the AIAA Aerospace Sciences Meeting*, AIAA SciTech Forum, Kissimmee, FL (AIAA, 2018-1400).

[34] C. Carton de Wiart and S. M. Murman, Assessment of wall-modeled les strategies within a discontinuous-galerkin spectral-element framework, in *Proceedings of the 55th AIAA Aerospace Sciences Meeting*, AIAA SciTech Forum, Grapevine, TX (AIAA, 2017-1223).

[35] L. T. Diosady and S. M. Murman, DNS of Flows over Periodic Hills using a Discontinuous Galerkin Spectral-Element Method, *44th AIAA Fluid Dynamics Conference*, AIAA Aviation Forum, Atlanta, GA (AIAA, 2014-2784).

[36] A. Garai, L. T. Diosady, S. M. Murman, and N. K. Madavan, High-pressure turbine cascade using a spectral-element discontinuous-Galerkin method, In *Proceedings of ASME Turbo Expo 2017, no. GT2017-64697*, Charlotte, NC (2017).

[37] M. Ceze, L. T. Diosady, and S. M. Murman, Development of a high-order space-time matrix-free adjoint solver, *54th AIAA Aerospace Sciences Meeting*, AIAA SciTech Forum, San Diego, CA (AIAA, 2016-0833).

[38] L. T. Diosady and S. M. Murman, Design of a Variational Multiscale Method for High Reynolds Number Compressible Flows, In *Proceedings of the 21st AIAA Computaional Fluid Dynamics Conference*, Fluid Dynamics and Co-located Conferences, San Diego, CA (AIAA, 2013-2870).

[39] L. T. Diosady and S. M. Murman, Higher-order methods for compressible turbulent flows using entropy variables, In *Proceedings of the 53rd AIAA Aerospace Sciences Meeting and Exhibit* (2015).

[40] P. Holmes, J. Lumley, and G. Berkooz, *Turbulence, Coherent Structures, Dynamical Systems and Symmetry* (Cambridge University Press, Cambridge, 1996).

[41] M. Farano, S. Cherubini, J.-C. Robinet, and P. De Palma, Optimal bursts in turbulent channel flow, J. Fluid Mech. **817**, 35 (2017).

[42] T. E. Oliphant, Python for Scientific Computing, Comput. Sci. Eng. **9**, 10 (2007).

[43] Q. Wang and J. Gao, The drag-adjoint field of a circular cylinder wake at Reynolds numbers 20, 100 and 500, J. Fluid Mech. **730**, 145 (2013).

[44] P. Mohan, N. Fitzsimmons, and R. D. Moser, Scaling of Lyapunov exponents in homogeneous isotropic turbulence, Phys. Rev. Fluids **2**, 114606 (2017).

[45] Q. Wang, R. Hui, and P. Blonigan, Least squares shadowing sensitivity analysis of chaotic limit cycle oscillations, J. Comput. Phys. **267**, 210 (2014).

[46] K. T. Alligood, T. D. Sauer, and J. A. Yorke, *Chaos: An Introduction to Dynamical Systems* (Springer, Berlin, 1996).